Chapter 6

Homogenization of elasto-viscoplastic composites

[1] In this section, another type of behavior for the constitutive phases of the composite is examined. More precisely, in addition to the elasto-plastic nature of the phases, the plastic regime exhibits a dependence with the loading rate. Such phenomena appear especially at high temperatures.

6.1 Constitutive equations

The Perzyna-type elasto-viscoplastic constitutive model is used for all the simulations presented in this work. However, the proposed homogenization technique for elasto-viscoplastic composites is not restricted to this single model. The following developments are limited to isotropic hardening in each phase.

The Perzyna-type constitutive model

The additive decomposition of the total strain gives an elastic part and an inelastic one, so that the time derivative of the Hookean's law can be rewritten

[1] Some developments of this chapter led to two publications "An enhanced affine formulation and the corresponding numerical algorithms for the mean-field homogenization of elasto-viscoplastic composites", Pierard O. and Doghri I., *International Journal of Plasticity*, 22 (2006), pp.131-157 [78] and "Micromechanics of particle-reinforced elasto-viscoplastic composites: finite element simulations versus affine homogenization", Pierard O., LLorca J., Segurado J. and Doghri I., *International Journal of Plasticity*, submitted for publication [82].

as:

$$\dot{\boldsymbol{\sigma}} = \boldsymbol{C} : (\dot{\boldsymbol{\varepsilon}} - \dot{\boldsymbol{\varepsilon}}^{in}). \tag{6.1}$$

As in elasto-plasticity, the inelastic strain rate is governed by a plastic flow rule:

$$\dot{\boldsymbol{\varepsilon}}^{in} = g_v \frac{\partial f}{\partial \boldsymbol{\sigma}} = \frac{3}{2} \frac{g_v}{\sigma_{eq}} \boldsymbol{\sigma}^{dev}, \tag{6.2}$$

where $g_v(\sigma_{eq}, p)$ is a viscoplastic function (see hereafter) which is equal to the plastic multiplier $\dot{\gamma}$ introduced for elasto-plasticity, f is the yield function ($f(\sigma_{eq}, p) = \sigma_{eq} - \sigma_Y - R(p)$) and is positive during plastic loading in the case of rate-dependent materials, σ_{eq} is the von Mises equivalent stress, σ_Y is the initial yield stress, $R(p)$ is the hardening stress (see hereafter), $\boldsymbol{\sigma}^{dev}$ is the deviatoric part of the stress tensor and p is the accumulated plasticity defined by (5.4). Combining these two relations leads to an equation linking stress and strain rates:

$$\dot{\boldsymbol{\sigma}} = \boldsymbol{C} : \left(\dot{\boldsymbol{\varepsilon}} - g_v(\sigma_{eq}, p) \frac{\partial f}{\partial \boldsymbol{\sigma}} \right). \tag{6.3}$$

Given this constitutive elasto-viscoplastic model, it is possible, for a homogeneous material, to predict the elasto-viscoplastic response. In order to compute the response of that material over a time step (the problem is supposed solved until the beginning of this time step) given either strain or stress increment, an algorithm is needed (e.g., (Doghri [24])) to solve two scalar equations by a Newton-Raphson scheme.

Hardening function

As in elasto-plasticity, the only hardening function considered in the subsequent simulations is a power-law model which is defined as:

$$R(p) = kp^n \text{ if } p > 0, \text{ 0 otherwise}, \tag{6.4}$$

where $k\,[Pa]$ is the hardening modulus and $n\,[-]$ the hardening exponent.

Viscoplastic function

The two viscoplastic functions defined hereafter require two parameters: the viscoplastic modulus (η [Pa.s] or κ [1/s]) and the viscoplastic exponent m [-].

- Norton's viscoplastic power law:

$$g_v(\sigma_{eq}, p) = \frac{\sigma_Y}{\eta} \left(\frac{\sigma_{eq} - \sigma_Y - R(p)}{\sigma_Y} \right)^m \text{ if } f > 0, \text{ 0 otherwise}. \tag{6.5}$$

- Viscoplastic power law as defined in ABAQUS [1]:
  This law is obtained by a slight modification of Norton's power law. Implementation of this law is useful for validation purposes.

$$g_v(\sigma_{eq}, p) = \kappa \left(\frac{\sigma_{eq} - \sigma_Y - R(p)}{\sigma_Y + R(p)} \right)^m \text{ if } f > 0, \text{ 0 otherwise.} \qquad (6.6)$$

6.2 Homogenization of elasto-viscoplastic composites

In elasto-viscoplasticity, there is no one-to-one correspondence between stress and strain rates through a so-called continuum tangent operator $\boldsymbol{C}^{ep}$ such as it exists in elasto-plasticity. It results that the incremental formulation of elasto-plastic composites (Hill [43]) cannot rigorously be used. However, when considering finite strain and stress increments instead of infinitesimal ones, an algorithmic tangent operator $\boldsymbol{C}^{alg}$ derived from a consistent linearization of the time-discretized constitutive equations exists in elasto-viscoplasticity (Ju [48], Doghri [24]):

$$\dot{\boldsymbol{\sigma}} \neq \boldsymbol{C}^{in} : \dot{\boldsymbol{\varepsilon}}, \qquad \boldsymbol{C}^{alg} = \frac{\partial(\Delta\boldsymbol{\sigma})}{\partial(\Delta\boldsymbol{\varepsilon})}. \qquad (6.7)$$

It is thus tempting to use a Hill-type incremental formulation nevertheless, but based on $\boldsymbol{C}^{alg}$. Unfortunately, as observed in various simulations, such an approach gives too stiff responses. Such as done nowadays in elasto-plasticity, some adjustments should be done in order to get accurate predictions with an incremental formulation (e.g.: Doghri and Ouaar [26], Doghri and Friebel [25], Doghri and Tinel [27]). In some cases, using the latter formulation in elasto-viscoplasticity with algorithmic tangent operators $\boldsymbol{C}^{alg}$ gives acceptable predictions (an example is given in section 6.4.1). Another widely used formulation is the secant one. Li and Weng [58, 59, 60] performed various interesting simulations by making use of a secant viscosity in the local constitutive laws. However, the secant formulation cannot handle some important cases such as unloading, cyclic loading and otherwise non-proportional loading histories. A non-classical formulation is thus needed and the so-called affine formulation adopted in this work transforms the problem into a fictitious linear thermo-elastic one which can be homogenized according to classical homogenization schemes. This approach was introduced by Molinari *et al.* [69] and improved by Masson [66].

In order to predict the overall behavior, a homogenization scheme is used. Such an approach is much faster than a purely numerical method (e.g.: finite elements), especially when dealing with real structures for which two meshes are needed at different scales. However, in order to validate this model, FE simulations performed on unit cells are also carried out.

6.3 The affine formulation

In this section, the affine homogenization introduced by Masson [66] is presented. Main steps of the linearization, predictions of the final response as well as an algorithm are detailed. Finally, a special attention is paid to the differences with previous implementations of this method.

The affine formulation relies on a linearization in time of the constitutive equations of the strain rate and the rate of internal variables. For clarity of the development, a single scalar internal variable p, not yet specified, is considered. When dealing with hereditary behaviors (such as in elasto-viscoplasticity), a direct prediction of the response is impossible and a discretization into time steps is required. During all the linearization procedure described hereafter, the problem is considered over a time step, for which the solution is supposed already found up to the beginning of the time step (t_n). For this, the constitutive model has to be written under the general form:

$$\dot{\boldsymbol{\varepsilon}}(t) = \underbrace{\boldsymbol{S} : \dot{\boldsymbol{\sigma}}(t)}_{\dot{\boldsymbol{\varepsilon}}^{el}(t)} + \dot{\boldsymbol{\varepsilon}}^{in}(\boldsymbol{\sigma}(t), p(t)), \tag{6.8}$$

$$\dot{p}(t) = \dot{p}(\boldsymbol{\sigma}(t), p(t)), \tag{6.9}$$

with $\dot{\boldsymbol{\varepsilon}}(t)$ the total strain rate, $\dot{\boldsymbol{\sigma}}(t)$ the Cauchy stress rate, $\dot{\boldsymbol{\varepsilon}}^{el}$ and $\dot{\boldsymbol{\varepsilon}}^{in}$ the elastic and inelastic strain rates, respectively, and $\boldsymbol{S}$ the elastic compliance tensor.

6.3.1 From elasto-viscoplasticity to linear thermo-viscoelasticity

The first step in the theory is a linearization of equations (6.8-6.9) around time t_n:

$$\dot{\boldsymbol{\varepsilon}}^{in}(t) = \dot{\boldsymbol{\varepsilon}}^{in}(t_n) + \boldsymbol{m}(\tau) : [\boldsymbol{\sigma}(t) - \boldsymbol{\sigma}(t_n)] + \boldsymbol{n}(\tau)[p(t) - p(t_n)], \tag{6.10}$$

$$\dot{p}(t) = \dot{p}(t_n) + \boldsymbol{l}(\tau) : [\boldsymbol{\sigma}(t) - \boldsymbol{\sigma}(t_n)] + q(\tau)[p(t) - p(t_n)], \tag{6.11}$$

in which four derivatives are introduced:

$$m_{ijkl} = \frac{\partial \dot{\boldsymbol{\varepsilon}}^{in}_{ij}}{\partial \sigma_{kl}}, \quad n_{ij} = \frac{\partial \dot{\boldsymbol{\varepsilon}}^{in}_{ij}}{\partial p}, \quad l_{kl} = \frac{\partial \dot{p}}{\partial \sigma_{kl}}, \quad q = \frac{\partial \dot{p}}{\partial p}. \tag{6.12}$$

These derivatives are evaluated at time τ, which belongs to the time interval $[t_n; t]$. Analytical expressions of these derivatives are available once the constitutive model is defined.

For the Perzyna-type constitutive model (section 6.1), these derivatives are

nil if the yield function is negative or nil. If $f > 0$, they are given by:

$$m_{ijkl} = \frac{\partial g_v}{\partial \sigma_{eq}} N_{kl} N_{ij} + g_v \frac{\partial N_{ij}}{\partial \sigma_{kl}} \quad , \qquad n_{ij} = \frac{\partial g_v}{\partial p} N_{ij},$$
$$l_{kl} = \frac{\partial g_v}{\partial \sigma_{eq}} N_{kl} \quad , \qquad q = \frac{\partial g_v}{\partial p}, \tag{6.13}$$

where:

$$\frac{\partial N_{ij}}{\partial \sigma_{kl}} = \frac{1}{\sigma_{eq}} \left[\frac{3}{2} I^{dev}_{ijkl} - N_{ij} N_{kl} \right]. \tag{6.14}$$

Derivative q is always negative, which is logical. If p increases, $R(p)$ increases also and since the stress is considered constant in this partial derivative, $f(\boldsymbol{\sigma}_{eq}, p)$ decreases. Thus, the viscoplastic function $g_v(\boldsymbol{\sigma}_{eq}, p)$ and $\dot{p}$ decrease so that $q = \frac{\partial \dot{p}}{\partial p}$ is negative.

As shown in appendix D.1, the solution of equation (6.11) can be given under the integral form:

$$p(t) - p(t_n) = \hat{p}(\tau, t) + \int_0^t e^{(t-u)q(\tau)} \boldsymbol{l}(\tau) : \boldsymbol{\sigma}(u) du, \tag{6.15}$$

where:

$$\begin{aligned} \hat{p}(\tau, t) \quad &= \quad q^{-1}(\tau)[e^{(t-t_n)q(\tau)} - 1][\dot{p}(t_n) - \boldsymbol{l}(\tau) : \boldsymbol{\sigma}(t_n)] \\ &\quad - \int_0^{t_n} e^{(t-u)q(\tau)} \boldsymbol{l}(\tau) : \boldsymbol{\sigma}(u) du. \end{aligned} \tag{6.16}$$

By inserting result (6.15) in equation (6.10) and after some mathematical manipulations (detailed proof in appendix D.2), the problem (6.10-6.11) is rewritten as:

$$\dot{\boldsymbol{\varepsilon}}(t) = \frac{d}{dt} \left[\int_0^t \boldsymbol{S}_\tau(\tau, t-u) : \dot{\boldsymbol{\sigma}}(u) du \right] + \dot{\boldsymbol{\varepsilon}}^0(\tau, t) = [\boldsymbol{S}_\tau \odot \dot{\boldsymbol{\sigma}}]_{(\tau,t)} + \dot{\boldsymbol{\varepsilon}}^0(\tau, t), \tag{6.17}$$

in which the Stieljes-type convolution product denoted by $\odot$ is introduced. Semi-analytical expressions of tensors $\boldsymbol{S}_\tau(\tau, t)$ and $\dot{\boldsymbol{\varepsilon}}^0(\tau, t)$ are reported in appendix D.2.

Rewriting local constitutive equations as (6.17) is remarkable as they become similar to linear viscoelastic ones, with an additive eigenstrain rate term. Classically, this problem is solved with the help of the Laplace-Carson transform as presented in the next section.

6.3.2 From linear thermo-viscoelasticity to linear thermo-elasticity

Similarly to the solution method proposed for linear viscoelastic materials (section 4.4.1), the Laplace-Carson transform (appendix B.1) is used to write equation (6.17) in a linear elastic form. Under this transformation, the Stieljes-type

convolution product becomes a single contraction so that the linearized constitutive law reads:

$$\begin{aligned} \dot{\boldsymbol{\varepsilon}}^*(s) &= \boldsymbol{S}^*_\tau(\tau,s) : \dot{\boldsymbol{\sigma}}^*(s) + \dot{\boldsymbol{\varepsilon}}^{0*}(\tau,s), && (6.18)\\ \text{or equivalently } \dot{\boldsymbol{\sigma}}^*(s) &= \boldsymbol{C}^*_\tau(\tau,s) : (\dot{\boldsymbol{\varepsilon}}^*(s) - \dot{\boldsymbol{\varepsilon}}^{0*}(\tau,s)), && (6.19)\\ \text{with } \boldsymbol{C}^*_\tau(\tau,s) &= \left[\boldsymbol{S}^*_\tau(\tau,s)\right]^{-1}, \end{aligned}$$

where an asterisk in exponent means the Laplace-Carson transform and s is the Laplace variable. $\boldsymbol{S}^*_\tau$ and $\dot{\boldsymbol{\varepsilon}}^{0*}$ are given by (proof in appendix D.3):

$$\boldsymbol{S}^*_\tau(\tau,s) = \boldsymbol{S} + \frac{\boldsymbol{m}(\tau)}{s} + \frac{\boldsymbol{n}(\tau)\otimes\boldsymbol{l}(\tau)}{s(s-q(\tau))}, \tag{6.20}$$

$$\begin{aligned} \dot{\boldsymbol{\varepsilon}}^{0*}(\tau,s) &= \dot{\boldsymbol{\varepsilon}}^{in}(t_n)e^{-s\tau} + s\int_0^{t_n} \dot{\boldsymbol{\varepsilon}}^{in}(t)e^{-st}dt \\ &\quad -s\boldsymbol{m}(\tau) : \int_0^{t_n} \boldsymbol{\sigma}(t)e^{-st}dt - \boldsymbol{m}(\tau) : \boldsymbol{\sigma}(t_n)e^{-st_n} \\ &\quad -q^{-1}(\tau)\dot{p}(t_n)\frac{se^{-st_n}}{q(\tau)-s}\boldsymbol{n}(\tau) \\ &\quad +q^{-1}(\tau)\left[\frac{s}{q(\tau)-s}+1\right]\boldsymbol{l}(\tau) : \boldsymbol{\sigma}(t_n)e^{-st_n}\boldsymbol{n}(\tau) \\ &\quad +q^{-1}(\tau)\boldsymbol{l}(\tau) : \boldsymbol{\sigma}(t_n)e^{-st_n}\boldsymbol{n}(\tau) \\ &\quad -q^{-1}(\tau)\dot{p}(t_n)e^{-st_n}\boldsymbol{n}(\tau) \\ &\quad +\frac{s}{q(\tau)-s}\boldsymbol{n}(\tau) : \boldsymbol{l}(\tau)\int_0^{t_n} \boldsymbol{\sigma}(t)e^{-st}dt \\ &\quad +\widehat{\boldsymbol{\varepsilon}}^{0*}(\tau,s,\boldsymbol{\sigma}(0)), \end{aligned} \tag{6.21}$$

$$\widehat{\boldsymbol{\varepsilon}}^{0*}(\tau,s,\boldsymbol{\sigma}(0)) = \boldsymbol{m}(\tau) : \boldsymbol{\sigma}(0) - \boldsymbol{n}(\tau)q^{-1}(\tau)\left(1-\frac{s}{s-q(\tau)}\right)\boldsymbol{l}(\tau) : \boldsymbol{\sigma}(0).$$

A proof of these expressions is given in appendix D.3. A special attention is paid to the computation at a low memory cost of these integrals so that they are always evaluated from variables at the end of the previous time step, which requires to decompose the integrals. Some details are given in appendices C and D. These equations are similar to those of linear thermo-elasticity. Of course, they are fictitious constitutive equations since they are defined in the Laplace-Carson domain. Classical homogenization schemes valid in linear thermo-elasticity can thus apply.

6.3.3 Algorithm

Consider now a two-phase elasto-viscoplastic composite for which constitutive equations of each phase can be linearized over a time interval as (6.19). Simi-

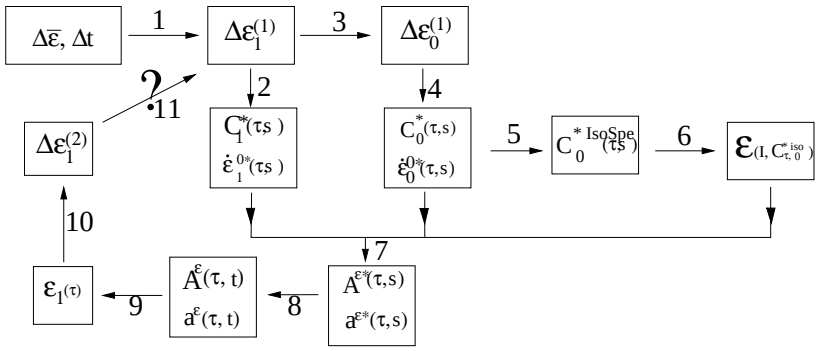

Figure 6.1: Iterative procedure to find the correct strain increments in the phases. Labels 1,. . . ,11 refer to the step numbers in the algorithm of section 6.3.3.

larly to linear thermo-elasticity, localization equation can be written as:

$$< \dot{\boldsymbol{\varepsilon}}^*(s) >_{\omega_1} = \boldsymbol{A}^{\epsilon *}(\tau, s) : \dot{\bar{\boldsymbol{\varepsilon}}}^*(s) + \boldsymbol{a}^{\epsilon *}(\tau, s), \tag{6.22}$$

Corresponding relation in the time domain writes:

$$< \boldsymbol{\varepsilon}(t) >_{\omega_1} = < \boldsymbol{\varepsilon}(0) >_{\omega_1} + [\boldsymbol{A}^{\epsilon} \otimes \dot{\bar{\boldsymbol{\varepsilon}}}]_{(\tau,t)} + \int_0^t \boldsymbol{a}^{\epsilon}(\tau, u) du, \tag{6.23}$$

where $\boldsymbol{A}^{\epsilon}$ and $\boldsymbol{a}^{\epsilon}$ are the strain localization tensors defined for the homogenization of two-phase linear thermo-elastic composites. In this section, an iterative procedure to determine strain increments in each phase over a time step is proposed. For this, consider the problem solved until the beginning of this time step, all local variables being known at that time. Over the time step $[t_n, t_{n+1}]$, a macro strain increment $\Delta\bar{\epsilon}$ is given. The algorithm is illustrated schematically on figure 6.1, main steps being described hereafter.

1. Initialization of the average strain increment $\Delta\boldsymbol{\varepsilon}_1$ in the inclusions with the converged value at the previous time step weighted by a possible variation of the time increment: $\Delta\boldsymbol{\varepsilon}_1 = \frac{t_{n+1}-t_n}{t_n-t_{n-1}}(\boldsymbol{\varepsilon}_1(t_n) - \boldsymbol{\varepsilon}_1(t_{n-1}))$.

2. Computation of the affine stiffness modulus $\boldsymbol{C}_1^*(\tau, s)$ and the eigenstrain tensor $\dot{\boldsymbol{\varepsilon}}_1^{0*}(\tau, s)$ in (6.19) in the reference inclusions' phase. For this, the response of the phase has first to be computed according to the constitutive model of the inclusions with $\Delta\boldsymbol{\varepsilon}_1$ as input. Secondly, one has to compute the derivatives of the evolution laws of inelastic strain rates and rate of plasticity with respect to their parameters (6.12). These are evaluated at time $\tau = t_{n+1}$. The discretization is done implicitly so that the

derivatives are evaluated at t_{n+1}. Finally, the required $\boldsymbol{C}_1^*(\tau, s)$ is computed by taking the inverse of expression (6.20) and $\dot{\boldsymbol{\varepsilon}}_1^{0*}(\tau, s)$ by using (6.21).

3. Evaluation of the corresponding strain increment in the matrix: $\Delta\boldsymbol{\varepsilon}_0 = \frac{1}{v_0}(\Delta\bar{\boldsymbol{\varepsilon}} - v_1\Delta\boldsymbol{\varepsilon}_1)$.

4. As in step 2, computation of the tensors $\boldsymbol{C}_0^*(\tau, s)$ and $\dot{\boldsymbol{\varepsilon}}_0^{0*}(\tau, s)$ for the matrix phase.

5. Extraction of the special isotropic part of $\boldsymbol{C}_0^*(\tau, s)$ as done for the incremental formulation in elasto-plasticity (section 5.3.3) - noted $\boldsymbol{C}_0^{*\,\mathrm{IsoSpe}}(\tau, s)$.

6. Computation of Eshelby's tensor $\mathcal{E}(I, \boldsymbol{C}_0^{*\,IsoSpe}(\tau, s))$ with $\boldsymbol{C}_0^{*\,IsoSpe}(\tau, s)$ and the inclusions shape (I) (appendix A.1).

7. Computation of the strain concentration tensors $\boldsymbol{A}^{\boldsymbol{\varepsilon}*}(\tau, s)$ and $\boldsymbol{a}^{\boldsymbol{\varepsilon}*}(\tau, s)$ in the Laplace domain (equations (4.25, 4.56b), $\boldsymbol{B}^{\epsilon}$ is given by the adopted homogenization scheme - see section 4.2.3).

8. Numerical Laplace inversion (see appendix B.2) of $\boldsymbol{A}^{\boldsymbol{\varepsilon}*}(\tau, s)$ and $\boldsymbol{a}^{\boldsymbol{\varepsilon}*}(\tau, s)$. To perform this operation, the strain concentration tensors of step 7 must be evaluated at several collocation points s_i in the Laplace-Carson domain. Limit values of these functions are needed for the inversion and are given in appendix D.4.

9. Evaluation of a new value of the average strain in the inclusions at $t = t_{n+1}$ according to relation (6.23). When using a collocation method as advocated for the numerical Laplace inversion, the corresponding time function is under a serial decomposition form so that the convolution product and the integral can be evaluated analytically (not too difficult for the integral and see appendix C for the incremental computation of the convolution product).

10. Computation of the average strain increment in the inclusions.

11. Comparison of this new value with the one at the beginning of this iteration. If it deviates too much, a new iteration is performed with this new value. Otherwise, the estimates per phase are accepted and the overall macroscopic response is computed as explained in section 6.3.4.

This algorithm is the core of the "Affinistan" software developed in the context of this thesis. A short presentation is given in appendix F.

6.3.4 Prediction of the macroscopic response

Once the average strain increments in each phase are found by the algorithm presented in section 6.3.3, there are two different ways to compute the macroscopic stress response corresponding to a macro strain increment.

The first method considers that the macroscopic stress is the spatial average of the local stresses, i.e. sum of the average stresses in the phases weighted by the corresponding volume fraction of that phase. This is easily done at a low computation cost.

The second method is based on a macroscopic linear viscoelastic relation. Indeed, in the linearization procedure, linear viscoelastic constitutive relations exist for each phase at each time step so that the macroscopic one at a given time step is form-similar:

$$\bar{\boldsymbol{\sigma}}(t_{n+1}) = \bar{\boldsymbol{\sigma}}(0) + \int_0^{t_{n+1}} \bar{\boldsymbol{C}}_\tau(\tau, t_{n+1} - u) : (\dot{\bar{\boldsymbol{\varepsilon}}}(u) - \dot{\bar{\boldsymbol{\varepsilon}}}^0(t_{n+1}, u))du. \qquad (6.24)$$

At first, computation of the homogenized tensors ($\bar{\boldsymbol{C}}^*(\tau, s)$ and $\dot{\bar{\boldsymbol{\varepsilon}}}^{0*}(\tau, s)$) in thermo-elasticity are needed. The numerical Laplace inversion back to the time domain (see appendix B.2) of these tensors give serial decompositions so that the convolution product can be computed analytically, and finally, the macroscopic stress response is computable.

This second approach is more time-consuming and requires two additional numerical inversions of the Laplace-Carson transform. Since some numerical errors appear in this inversion and the method is sensitive to the choice of the collocation points (see appendix B.2), the quality of the final prediction might be better with the first method. For example, using (6.24) introduces some fictitious plasticity during elastic unloading or reloading. The two methods have been implemented and with a minimum of care with the numerical Laplace inversions, no significant differences on the predictions have been observed. Logically, for performance reasons, the first option is the default one.

If there are constraints on the corresponding macroscopic stress tensor (e.g.: uniaxial tension, biaxial tension, shear,...), an additive iterative loop is necessary and is described in appendix E. For this purpose, several components of the macroscopic tangent operator are needed. This is done with a perturbation method.

6.3.5 Main differences with previous implementations

The major differences in our implementation with previous ones (Brenner *et al.* [15], Masson and Zaoui [68], Masson *et al.* [67]) are the following:

- A full treatment of the evolution laws of internal variables, e.g.: accumulated plasticity for composite materials or resistances of the slip systems

for polycrystals. This consideration adds a great deal of complexity to the mathematical developments of the affine formulation.

- This work is focused on two-phase composites, on the contrary to Masson [66] who studied various crystalline symmetries and especially Zirconium's alloys modeled as polycrystals. The fact that we consider a different microstructure does not have an impact on the development of the affine formulation itself, but on the constitutive models of the phases and most importantly on the numerical algorithms which have to be robust in order to handle different constitutive models and contrasts between phase materials.

- An extensive validation of the method. Up to now, very few validations were available.

- Simulations are performed under various loading cases. To our knowledge, no one has performed cyclic loading tests with an affine formulation before.

It should be noted that two extensions of the affine formulation have been developed by Brenner *et al.* [14]. First one deals with a simplified numerical Laplace-Carson transform. Such approach enables to reduce the required computation time for this operation and is especially useful for polycrystals due to the numerous different grains. The other extension takes into account the second order moment of the stress tensor in the definition of the reference state. This is done for polycrystals which exhibit a power law constitutive law. In this case, the secant and affine moduli are linked in a simple way so that the evaluation of the second order moment of the stress tensor can be obtained in a semi analytical fashion.

6.4 Numerical simulations

6.4.1 General simulations

In this first part of the numerical simulations of the affine formulation, a wide range of loading paths, homogenization methods and comparisons with another formulation are presented. In the description of the material properties, subscript 0 refers to the matrix and 1 to the inclusions.

Effect of the homogenization formulation In the past, the incremental formulation has been criticized for giving too stiff predictions. Extracting the isotropic part of the algorithmic tangent modulus leads to much more realistic predictions in the elasto-plastic regime (Doghri and Ouaar [26]). As mentioned

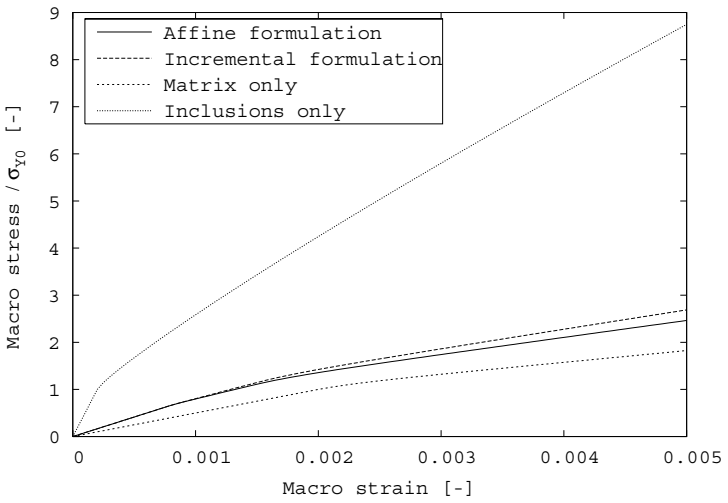

Figure 6.2: Uniaxial tension test. Comparison of the affine and incremental formulations.

in section 6.2, the incremental formulation cannot rigorously be used in the rate-dependent case because of the absence of continuum tangent operators relating strain and stress rates. Nevertheless, since an algorithmic tangent operator $\boldsymbol{C}^{alg}$ -equation (6.7b)- can be defined, the idea in this section is to run the incremental formulation in elasto-viscoplasticity with $\boldsymbol{C}^{alg}$ although there is no constitutive justification for $\boldsymbol{C}^{alg}$. The predictions will be compared to those of the affine formulation.

Material properties of the considered two-phase composite are the following (Norton's viscoplastic power law is used): $E_0 = 50$ GPa, $\nu_0 = 0.3$, $\sigma_{Y_0} = 100$ MPa, $k_0 = 50$ GPa, $n_0 = 1.0$, $\eta_0 = 30.0$ GPa.s and $m_0 = 1.0$ for the matrix which is reinforced by 30% of spherical inclusions with the following properties: $E_1 = 500$ GPa, $\nu_1 = 0.3$, $\sigma_{Y_1} = 100$ MPa, $k_1 = 100$ GPa, $n_1 = 0.85$, $\eta_1 = 10.0$ GPa.s and $m_1 = 1.0$. This composite undergoes a uniaxial tension test at a constant strain rate of 10^{-3} s^{-1}.

Predictions obtained with the two formulations are reported on figure 6.2, as well as responses of individual phases alone. As expected, this test shows that the prediction of the affine formulation is softer than that of the incremental one, although in this example the difference is not too pronounced.

Effect of the inclusions shape A major advantage of Eshelby-based homogenization schemes is that they can predict the influence of the shape of the inclusions. In this test, predictions of two composites made of the same

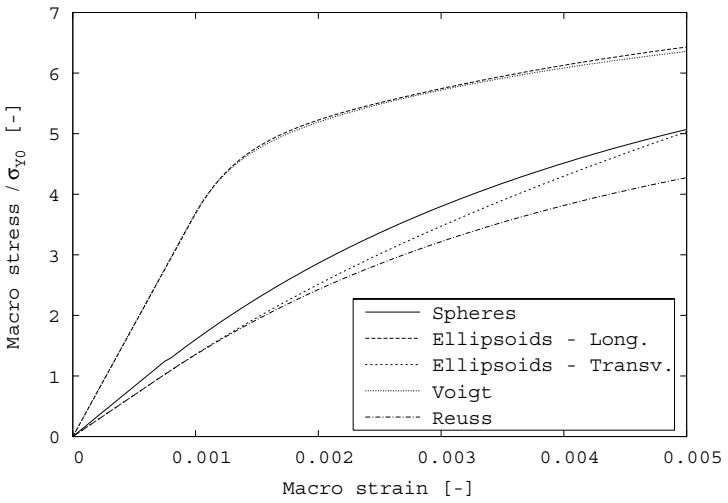

Figure 6.3: Uniaxial tension test in the longitudinal and transverse directions. Influence of the reinforcements shape.

materials are compared, one being reinforced with spheres, the other by long fibers. These results are confronted to the bounds of Reuss and Voigt (which are independent of the reinforcements shape).

In this test, the contrast between the phases is more pronounced : $E_0 = 100$ GPa, $\nu_0 = 0.3$, $\sigma_{Y_0} = 100$ MPa, $E_1 = 1000$ GPa, $\nu_1 = 0.3$ and $\sigma_{Y_1} = 1000$ MPa. Both phases obey a power law hardening function and Norton's viscoplastic law ($k = 10$ GPa, $n = 1$, $\eta = 300$ GPa.s and $m = 1$). The uniaxial tension test is performed at a constant strain rate of 10^{-3} s^{-1}. For both composites, the volume fraction of the inclusions is 30%.

Logically, as illustrated on figure 6.3, the composite made with fibers has, in the longitudinal direction, a much better resistance to this traction test than the composite reinforced by spheres. On the contrary, the response in the transverse direction of the composite reinforced by fibers is softer than the one of the composite made with spheres. One can note that the response of the long fiber composite predicted with Mori-Tanaka in the direction of the fibers is slightly stiffer than with Voigt! This is due to some small numerical errors occurring in the Laplace inversion as explained in appendix B.2. The Reuss and Voigt schemes avoid these problems since inversions of the constant strain concentration tensors are obvious.

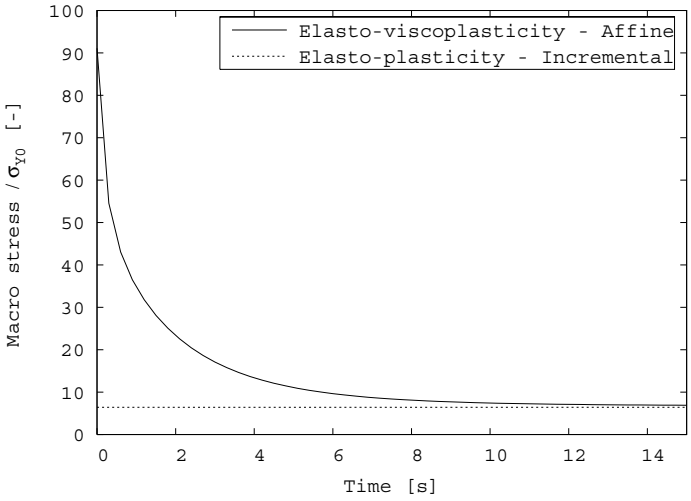

Figure 6.4: Uniaxial relaxation test of a long fiber reinforced composite in the longitudinal direction. Illustration of the viscous effects.

Relaxation test In this relaxation test, the influence of the viscous effects is illustrated. Transient viscous effects of the studied composite is compared to the rate independent response of this composite.

The properties of this composite are the following: $E_0 = 100$ GPa, $\nu_0 = 0.2$ and $\sigma_{Y_0} = 100$ MPa for the matrix, $E_1 = 500$ GPa, $\nu_1 = 0.3$ and $\sigma_{Y_1} = 500$ MPa for the inclusions. For both phases, the power law hardening model is defined by $k = 10$ GPa and $n = 1$. The Norton's viscoplastic laws have different parameters for each phase: $\eta_0 = 300$ GPa.s, $n_0 = 1.1$ for the matrix and $\eta_1 = 500$ GPa.s, $n_1 = 1.8$ for the long fibers. The composite is reinforced by long fibers (20% of volume fraction) aligned with the direction of uniaxial relaxation.

On figure 6.4, initial stress response of the rate-dependent composite is the homogenized elastic one. Furthermore, it is observed at long times that the response of the composite tends to the instantaneous elasto-plastic one, which is obtained by the commercial software DIGIMAT [23]. This result is also obtained with homogenization methods but with an incremental formulation in elasto-plasticity.

Effect of the loading strain rate This simulation illustrates the influence of the loading strain rate in a shear test. For decreasing strain rates, responses become softer and should tend to the rate independent one.

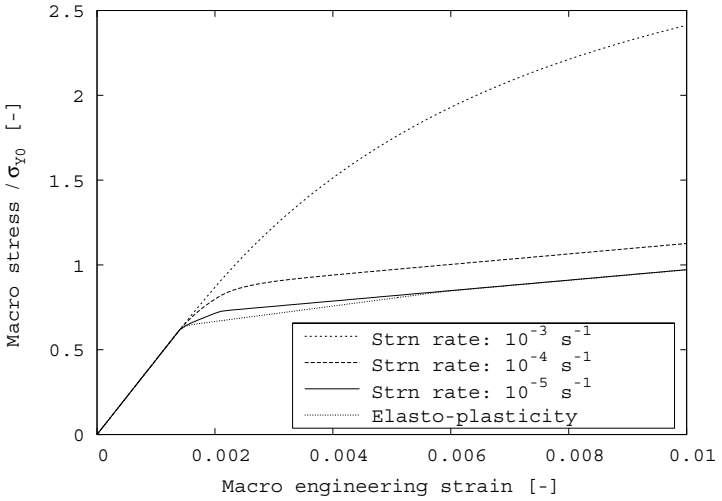

Figure 6.5: Sphere-reinforced composite under a shear test. Influence of the loading strain rate.

The two phases of this composite obey to power law hardening model and Norton's viscoplastic law. Mechanical properties are the following: $E_0 = 100$ GPa, $E_1 = 200$ GPa, $\nu_0 = \nu_1 = 0.3$, $\sigma_{Y_0} = 100$ MPa, $\sigma_{Y_1} = 200$ MPa, $k_0 = k_1 = 10$ GPa, $n_0 = n_1 = 1$, $\eta_0 = \eta_1 = 300$ GPa.s and $m_0 = m_1 = 1$. The volume fraction of spherical inclusions is 20 %.

Responses of the rate-dependent composite at various strain rates are plotted on figure 6.5. For comparison, the rate independent response computed with the commercial program DIGIMAT [23] is also reported. Simulation at the lowest strain rate (10^{-5} s^{-1}) is almost identical to the elasto-plastic response since hardening introduced by the strain rate is negligible while at higher strain rates, the response becomes logically stiffer. At low strain rates, the prediction doesn't drop below this rate independent limit, even if these two responses are obtained with two completely different approaches. However, at very low strain rates (order of 10^{-10} s^{-1}), numerical instabilities arise and a lack of precision is observed in the affine formulations.

6.4.2 Validation against 3D finite element simulations

As second part of the numerical validations of the affine formulation, confrontations are made against 3D FE simulations. Per phase analysis is also performed in order to better understand the limits of the method.

Throughout this section, only one material is considered in order to get more

relevant interpretations. This is a two-phase elasto-viscoplastic composite with a hardening power law (section 6.1) and the rate-dependent power law defined in ABAQUS (section 6.1). According to the notations previously introduced, the parameters are the following: $E_0 = 70$ GPa, $\nu_0 = 0.33$, $\sigma_{Y0} = 70$ MPa, $k_0 = 4$ GPa, $n_0 = 0.4$, $\kappa_0 = 3\,10^{-4}$ s^{-1} and $m_0 = 1.5$ for the matrix and $E_1 = 400$ GPa, $\nu_1 = 0.286$, $\sigma_{Y1} = 400$ MPa, $k_1 = 8$ GPa, $n_1 = 0.4$, $\kappa_1 = 2\,10^{-4}$ s^{-1} and $m_1 = 1.5$ for the spherical inclusions.

Finite element simulations are performed on 3D unit cells reinforced by several dozens of spheres. These are randomly distributed in the unit cell and periodic boundary conditions are enforced. Isotropy of the cells and low scattering between predictions obtained on several cells have been checked. Computation time was much higher than for an elasto-plastic matrix reinforced by elastic inclusions: about six hours on a HP RX-4640 with four processors and 8 Gb of RAM instead of one and an half hour.

Effect of the volume fraction and strain rate Predictions at different strain rates on a cell containing 15% of reinforcements are illustrated on figure 6.6a. For this, 6 FE simulations are performed at an average strain rate and conditions (cell and tension direction) of the closest response to the average one are used at the other strain rates. The response obtained by the incremental formulation for rate independent elasto-plastic materials is also reported. As previously, simulation at the lowest strain rate (10^{-6} s^{-1}) is almost identical to the elasto-plastic response. One can observe that at low strain rates, predictions with the affine formulation coincide almost perfectly with the FE simulations. At higher strain rates, the final response diverges a little bit from the reference results, predictions with the homogenization scheme being a little bit softer. This underestimation, which is unusual for homogenization schemes, is partly due to the use of the isotropic extraction of the affine modulus of the matrix ($\boldsymbol{S}_\tau^{*^{-1}}$) to compute the Eshelby's tensor. As illustrated on figure 6.6b, comments for cells containing twice more reinforcements (30%) are similar, the difference at high strain rates being more pronounced while predictions at low strain rates remain very good. Increasing the volume fraction or the strain rate thus decreases the accuracy of the predictions by the affine formulation of homogenization.

Effect of triaxiality In this section, the influence of the triaxiality level is examined: shear, uniaxial tension or biaxial tension test. Since the affine homogenization scheme considers only average strain and stress fields to define the state of each phase, these will always be isotropic under a triaxial tension test on a cell reinforced by spheres (if the same tension is applied in the three directions). Since the Perzyna-type constitutive model considered here is based on the von Mises equivalent stress, no plasticity will appear. Obviously, this

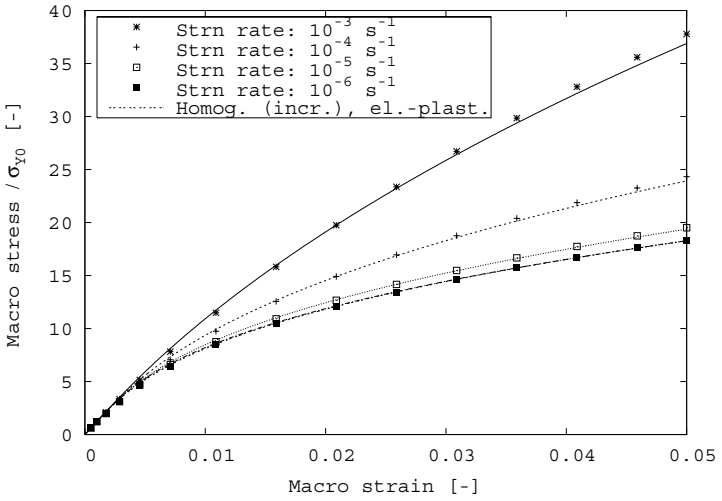

(a) Cell reinforced by 15% of stiff elasto-viscoplastic spherical inclusions.

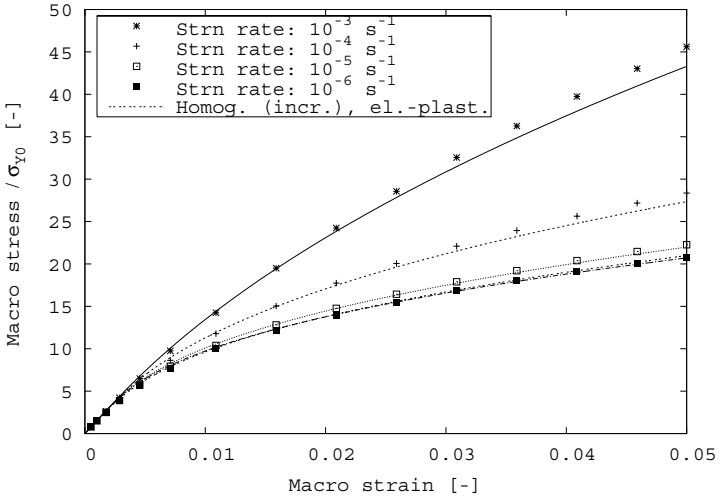

(b) Cell reinforced by 30% of stiff elasto-viscoplastic spherical inclusions.

Figure 6.6: Uniaxial tension test. Comparison between direct 3D FE analysis (points) and affine homogenization formulation (straight lines) for various strain rates.

is not correct. Indeed, some stress concentration will occur in the surrounding of the inclusions which will not be under a triaxial tension, so that plasticity

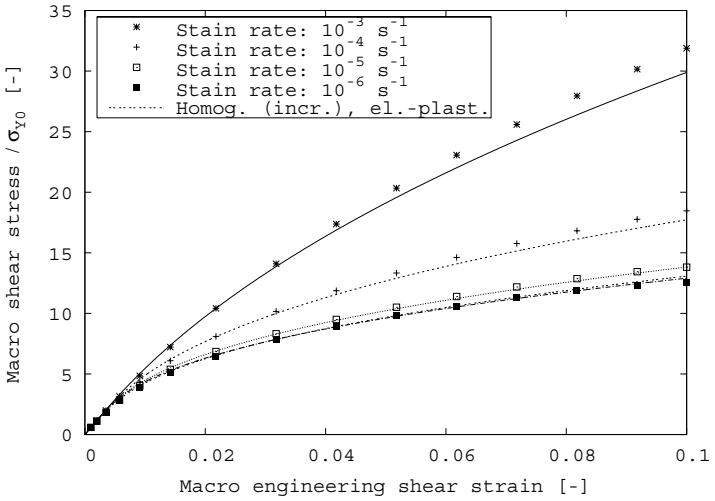

Figure 6.7: Shear test - cell reinforced by 30% of stiff elasto-viscoplastic spherical inclusions. Comparison between direct 3D FE analysis of RVE (points) and affine homogenization formulation (straight lines).

might develop. A good way to improve the model would be to take into account the second-order moment of the stress tensor which gives additional information on the heterogeneity of the stress field. For the other loading cases, it is interesting to know the triaxiality levels at which homogenization schemes give good predictions.

Let's consider at first shear tests at different strain rates. Results are reported on figure 6.7 for a cell reinforced by 30% of spheres. As in previous observations, good predictions are obtained at low strain rates and the relative difference between homogenization and reference FE results reaches about 5% as the strain rate increases. Similar results and interpretation are obtained for biaxial tension tests as illustrated on figure 6.8.

In order to check the accuracy of the triaxiality effect, von Mises equivalent stress versus equivalent strain is plotted for the different loading cases. These are computed as:

$$\boldsymbol{\sigma}_{eq} = \left(\frac{3}{2}\boldsymbol{\sigma}^{dev} : \boldsymbol{\sigma}^{dev}\right)^{1/2}, \qquad \boldsymbol{\varepsilon}_{eq} = \left(\frac{2}{3}\boldsymbol{\varepsilon}^{dev} : \boldsymbol{\varepsilon}^{dev}\right)^{1/2}, \tag{6.25}$$

where $\boldsymbol{\varepsilon}^{dev}$ is the deviatoric strain tensor. In FE, these values are computed from the volume average of the equivalent strain and equivalent stress fields. The comparison is reported on figure 6.9 for the different loading cases at

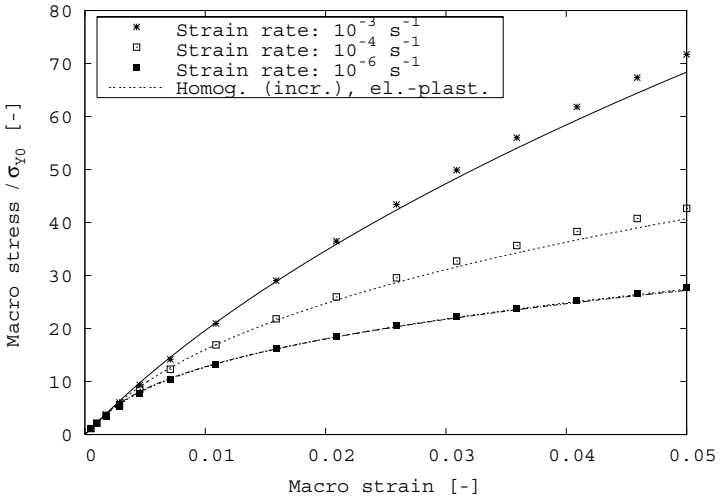

Figure 6.8: Biaxial tension test - cell reinforced by 30% of stiff elasto-viscoplastic spherical inclusions. Comparison between direct 3D FE analysis of RVE (points) and affine homogenization formulation (straight lines).

the highest strain rate ($10^{-3}\ s^{-1}$). Results do not have to be compared in a quantitative way but only the relative errors at the end of the simulations, which are at the last FE result of each curve: shear: 6.1%, uniaxial tension: 6.3% and biaxial tension: 3.9%. All these values are quite similar and by no way a deterioration of the predictions is observed as the level of triaxiality increases.

Effect of Cyclic loading In this section, strain rate effect is studied over a complete cycle of uniaxial loading/unloading/compression/reloading. The maximum macro strain at the end of loading, compression and reloading is $\pm$ 5%. On the contrary to homogenization schemes based on the secant formulation, the affine one enables such a non-monotonic loading.

Figure 6.10 reports simulations at two different strain rates over a complete cycle. The first loading path is exactly the same as the previously studied monotonic uniaxial loading case. During unloading and reloading, results at low strain rate of homogenization schemes and FE are almost identical, which is a pretty impressive result for such a high volume fraction of inclusions (30%). On the contrary, at high strain rates, the difference already observed at the end of the first loading path continues to increase during unloading and reloading.

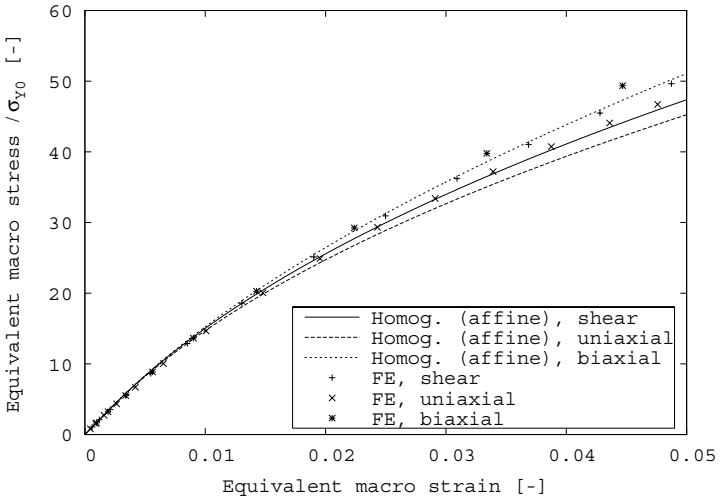

Figure 6.9: Influence of triaxiality - comparison of various loading tests (30% of inclusions).

One can observe that this difference does increase only during plastic increments but not during the elastic transitions.

Per phase analysis Even if a very good accuracy is observed for wide range of simulations, it has been observed that there is a systematic worsening of the predictions at high strain rates, the response becoming too soft under these conditions. Even if this is not a catastrophic effect, it is interesting to go deeper and understand the reasons of such a behavior. This will be done with the help of the numerical FE simulations. Effectively, these enable to get helpful information of the microscopic fields within each constituent of the composite.

A first source of error could come from the adopted homogenization scheme (Mori-Tanaka). This is known for giving good predictions at low volume fractions of the reinforcement phase but is less satisfying at higher ones. Effectively, an effect of the volume fraction of particles has been observed (figures 6.6a - 6.6b). However, differences between FE and mean-field predictions are noticeable only at high volume fractions so that this cannot explain the strain rate effect.

Another source of error might come from the definition of per phase reference states for homogenization schemes. In our implementation of the affine formulation, the reference equivalent stress is evaluated from the average stress tensor instead of the volume average of the equivalent stress field. Significative

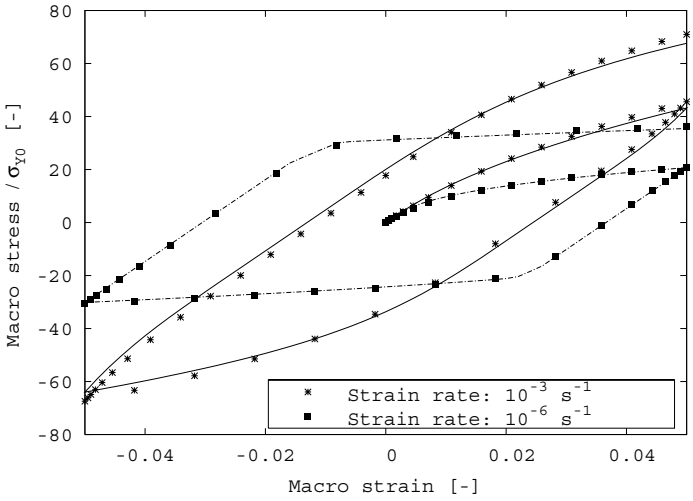

Figure 6.10: Cyclic uniaxial tension - compression test on a cell reinforced by 30% of stiff elasto-viscoplastic spherical inclusions. Comparison between direct 3D FE analysis of RVE and affine homogenization formulation. Specified strain rates are for the two loading paths while their opposites are used for unloading.

differences between these two evaluations exist for high levels of heterogeneity of the fields. This is illustrated on figure 6.11 for the accumulated plasticity for a cross section of the RVE at the end of one cycle of uniaxial loading. Especially in the matrix, the non uniformity is evident and is particularly high along the direction of traction (direction 1) where inclusions are close to each others. With the help of the local fields obtained by FE, the volumetric cumulative probability of accumulated plastic strain (volume fraction of a phase where the local accumulated plastic strain is smaller than a given value) enables to give a qualitative measure of the heterogeneity level. This is plotted at the end of the first cycle on figure 6.12*a* for the matrix and 6.12*b* for the inclusions. In both phases, the accumulated plastic strain is lower at high strain rates due to the stiffer response as the strain rate increases. Also, accumulated plastic strain is much more homogeneous at high strain rates than at lower ones. This would suggest that deterioration of the quality of the predictions at high strain rates is not linked to heterogeneity effects. Since precision is much better in the matrix, extending the affine formulation by taking into account second-order moments of the stress tensor would not increase significantly the quality of the predictions.

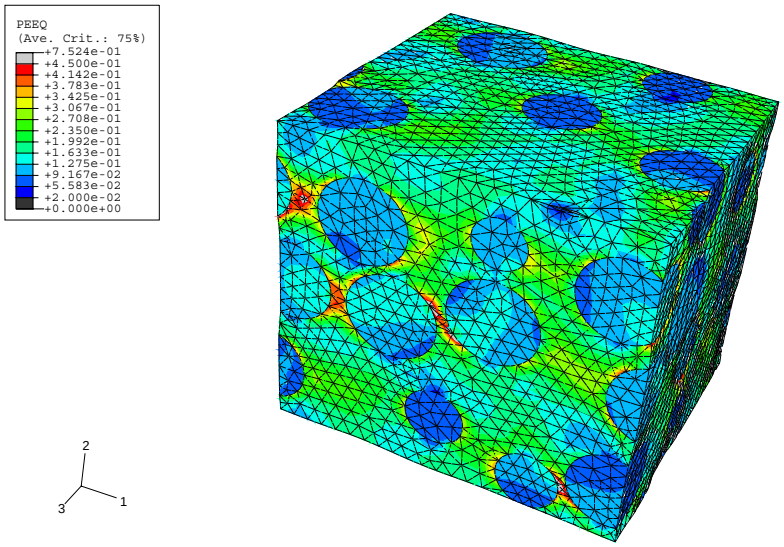

Figure 6.11: Cyclic uniaxial tension - compression test - cell reinforced by 30% of stiff elasto-viscoplastic spherical inclusions. Contour plot of the accumulated plastic strain field.

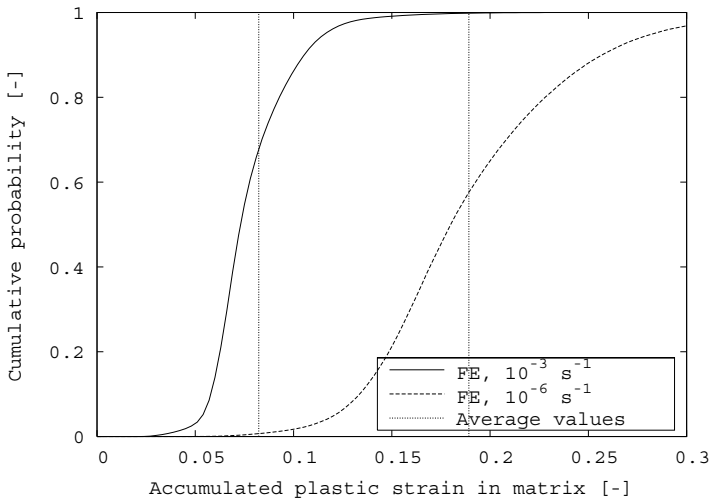

(a) Cumulative probability in the matrix.

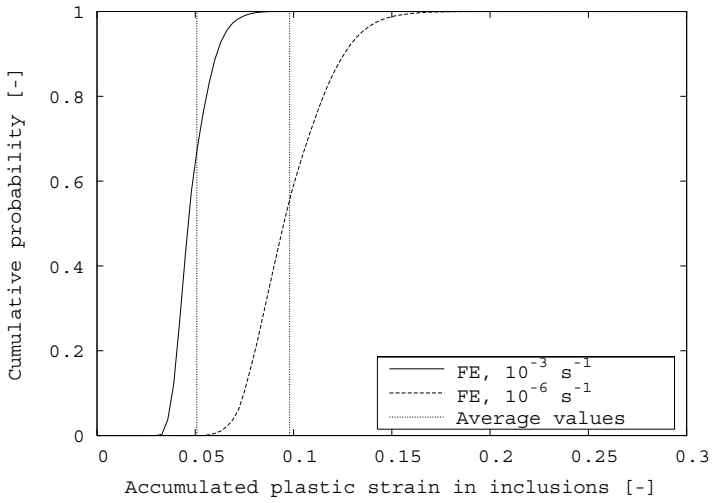

(b) Cumulative probability in the inclusions.

Figure 6.12: Measurement of the heterogeneity of the accumulated plastic strain field at the end of one cycle of uniaxial tension-compression.

An analysis of the per phase reference stresses is now performed. For the affine formulation, these are given from the average stress in the phase. For the FE simulations, relation (5.60) enables to compute the volume average of the

$\dot{\varepsilon}$ $[s^{-1}]$	Predictive method	p [-] in matrix	p [-] in incl.
10^{-6}	FE	0.1892	0.0980
	Homogenization	0.1949	0.0653
10^{-3}	FE	0.0823	0.0508
	Homogenization	0.0818	0.0394

Table 6.1: Accumulated plastic strain in the matrix and the inclusions at low and high strain rates obtained by homogenization and FE (volume average of the local field) at the end of one cycle.

equivalent stress in matrix. Similarly, this can be computed in the inclusions. These are plotted on figure 6.13 for a matrix reinforced by 30% of inclusions. This shows that the reference stress in the inclusions is underestimated while the ones in the matrix are acceptable. This observation is even more pronounced at high strain rates (figure 6.13b). Consequently, the accumulated plastic strain in the spherical inclusions given by the affine model is also underestimated (table 6.1). This result is surprising because it should lead to an overestimation of the stiffness of inclusions, which should lead to the same result for the composite. However, the effective composite behavior given by the affine model follows the opposite trend, so the differences between the model and the simulations cannot be attributed to this factor.

As explained in sections 5.3.1 and 6.3.3, a general implementation of the incremental and affine formulation gives too stiff macroscopic predictions. In order to solve this problem, various methods to reduce the matrix stiffness have been proposed (5.3.6). The one adopted for the affine formulation was to use an isotropic extraction of the matrix modulus for the computation of the Eshelby's tensor only while all the other computations are made with the anisotropic tensor. This technique is denoted *EshIso* in the following. Other stiffness reduction methods which gave satisfying results in elasto-plasticity (section 5.4.1) are to use this isotropic tensor for the computation of the Hill's tensor (*PIso*) only or for all the computations (*AllIso*). Such isotropisation techniques might have a considerable impact on the final prediction. Effective responses of these three methods are reported on figure 6.14a (volume fraction: 30%, strain rate: 10^{-3} s^{-1}). This shows that the adopted isotropisation (*EshIso*) underestimates the macroscopic predictions (as observed on figure (6.6b)) and the two other methods (*PIso* and *AllIso*) give slightly better results. The differences in the predictions are closely related to the evaluation of the reference stress in each phase as illustrated on figures 6.14b-6.14c. Very good accuracy of the predictions in the matrix are preserved whatever isotropisation technique is used while this is strongly improved in the inclusions by using either *PIso* or *All Iso*. Once again, this shows the crucial issue of a good choice of the affine modulus (isotropic or not) of the matrix to obtain accurate predictions of the effective

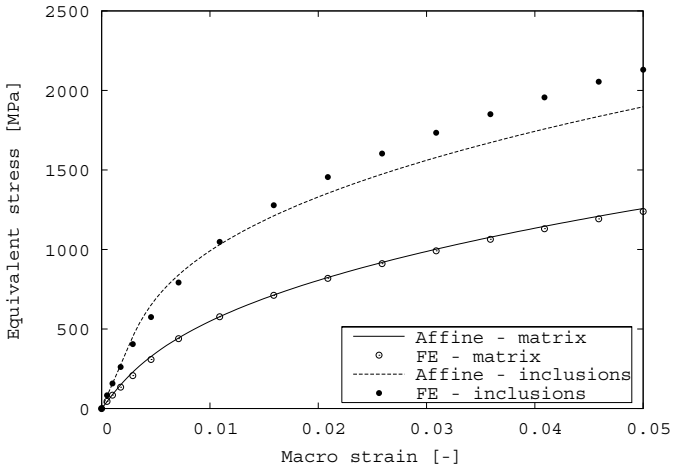

(a) Strain rate: 10^{-6} s^{-1}.

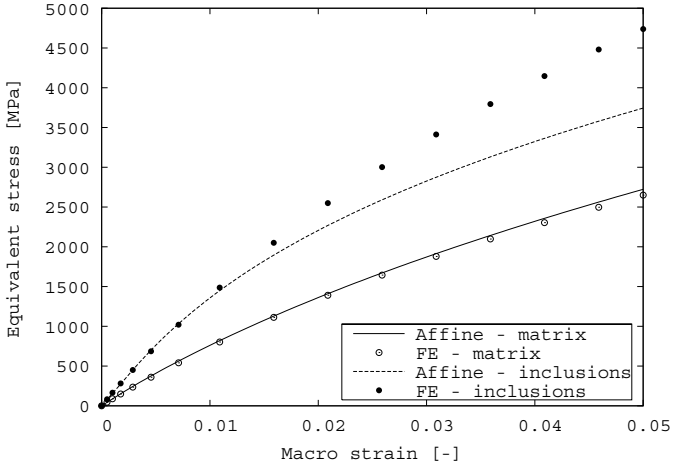

(b) Strain rate: 10^{-3} s^{-1}.

Figure 6.13: Evolution of the von Mises equivalent stress in both phases.

properties.

Finally, it should be noted that the collocation points needed for the numerical inversion of the Laplace transform in the simulations presented in figure 6.14 are slightly different than those used in all previous simulations in this chapter in order to better take into account the interaction law. This numerical modification (which only has a small influence if the isotropic part of the affine moduli

is only used to compute Eshelby's tensor) is necessary to obtain accurate results when Hill's tensor is computed with these isotropic moduli. Unfortunately, the mixture of very large times and very low collocation points leads to numerical problems at low strain rates and the non-linear localization tensorial equation (6.22) cannot be solved. Thus, for practical purposes, the affine homogenization model based on the isotropic projection of the affine modulus to compute only Eshelby's tensor has to be used to simulate the mechanical response of elasto-viscoplastic composites.

6.5 Conclusions

This chapter dealt with the affine formulation in the context of elasto-viscoplasticity. This formulation linearizes each phase's elasto-viscoplastic constitutive model into a fictitious linear thermo-elastic relation defined in the Laplace-Carson domain. At this stage, classical homogenization schemes valid in thermo-elasticity can be applied, from which the macroscopic response can be computed at the end of the time step. Our implementation includes a complete treatment of the internal variables.

The method enables to deal with various loadings, including cyclic, shear and relaxation tests. Influence of the shape of the reinforcements, the way to compute the macroscopic response and the influence of the homogenization scheme were also presented. Other simulations illustrate the viscous effects and when these become negligible, the elasto-plastic response is well retrieved.

The accuracy of the affine homogenization method was assessed by comparison with results obtained by the numerical simulation of a three-dimensional representative volume element of the composite microstructure. Macroscopic predictions of the affine homogenization model were excellent in composites with different volume fraction of spheres, subjected to different loading conditions as well as to monotonic and cyclic deformation, particularly at low strain rates. However, accuracy of the predictions decreased systematically as the strain rate increased, the homogenization scheme giving a slightly softer response than the numerical simulations. The detailed information of the stress and strain microfields given by the finite element simulations was used to analyze the source of this error, which was traced to the use of an isotropic extraction of the matrix affine modulus to compute Eshelby's tensor. It was found that better predictions at high strain rates could be obtained if the same isotropic extraction was used to determine Hill's tensor (instead of Eshelby's tensor) but the numerical problems associated with the numerical inversion of the Laplace-Carson transform did not make advisable to use this latter approach.

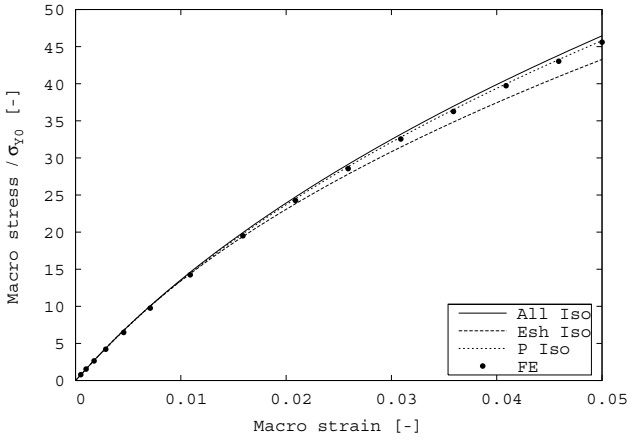

(a) Macroscopic predictions.

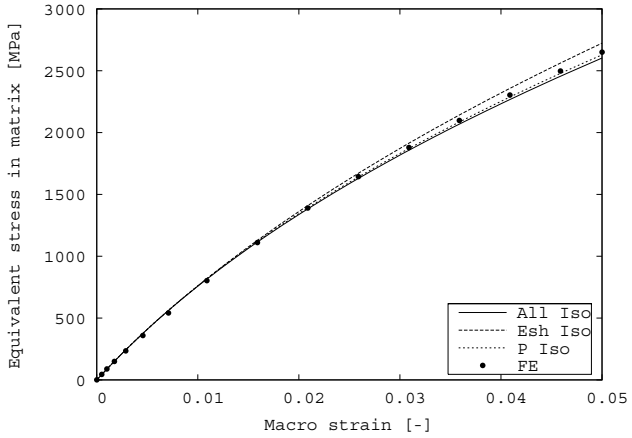

(b) Predictions in the matrix.

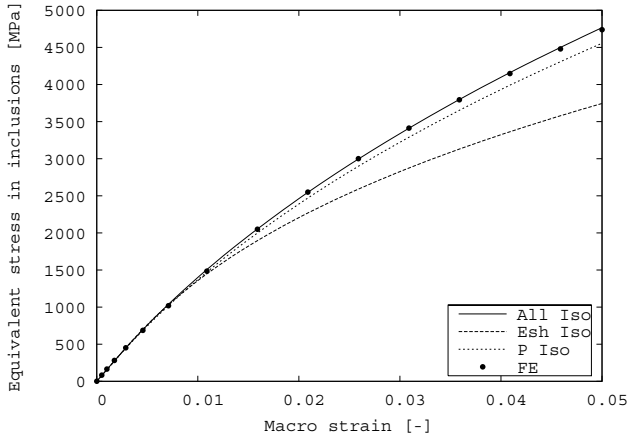

(c) Predictions in the inclusions.

Figure 6.14: Comparison of various isotropisation methods.